# Equivalent-Source Acoustic Holography for Projecting Measured Ultrasound Fields Through Complex Media

Bradley Treeby, *Member, IEEE*, Felix Lucka, Eleanor Martin, and B. T. Cox

***Abstract*— Holographic projections of experimental ultrasound measurements generally use the angular spectrum method or Rayleigh integral, where the measured data are imposed as a Dirichlet boundary condition. In contrast, full-wave models, which can account for more complex wave behavior, often use interior mass or velocity sources to introduce acoustic energy into the simulation. Here, a method to generate an equivalent interior source that reproduces the measurement data is proposed based on gradient-based optimization. The equivalent-source can then be used with full-wave models (for example, the open-source k-Wave toolbox) to compute holographic projections through complex media including nonlinearity and heterogeneous material properties. Numerical and experimental results using both time-domain and continuous-wave sources are used to demonstrate the accuracy of the approach.**

***Index Terms*— Equivalent source, full-wave modeling, gradient-based optimization, holography.**

## I. Introduction

ACOUSTIC holography is widely used in ultrasonics for reconstructing the 3-D acoustic field of an ultrasound transducer from hydrophone measurements made in a single plane [1], [2]. Given appropriate measurement conditions, field projections have been shown to agree closely with experimental measurements for both time-domain (i.e., broadband) and continuous-wave (CW) data [3]–[5]. The projections are typically performed using the angular spectrum method (ASM) or the Rayleigh integral [1]. Although formulated in different ways, both of these approaches project the measured field through a homogeneous medium based on the free-space Green's function for the wave equation (or Helmholtz equation for CW fields). This is equivalent to solving the wave equation for a homogeneous medium in a half-space subject to a planar, time-varying, Dirichlet boundary condition given by the measured acoustic pressure. These methods work very effectively for homogeneous media, but do not allow for projection of the measured data through complex media, e.g., with acoustic nonlinearity and spatially varying sound speed or mass density. Such simulations are of particular interest in medical ultrasonics as the acoustic properties of biological tissue are spatially varying, the wave propagation can be nonlinear, and it is often of interest to study the field of a particular transducer *in vivo* [6]–[8].

Numerical models that account for wave behavior in complex nonlinear media by directly solving the heterogeneous wave equation or the corresponding first-order conservation equations are available [9]–[11]. Due to the large size of the domain of interest compared to the acoustic wavelength [12], these models are generally based on computationally efficient collocation methods, e.g., finite-difference time domain or pseudospectral time-domain methods. The straightforward way to use these models for holography would be to define a time-varying Dirichlet boundary condition using the measured data. However, formulating arbitrary, time-varying boundary conditions that are accurate, stable, and retain the efficiency of these methods is far from trivial [13]. Instead, absorbing boundary conditions are usually imposed, and acoustic energy is introduced through interior sources. Therefore, to use these models for holography, it is necessary to find a mapping from the required time-varying Dirichlet boundary condition (the measured data) to interior sources that can be implemented in the model. One approach is to use the measured data to directly replace the local pressure values at each time step in the numerical simulation [14]. Both forward and back projections are possible by time-reversing the measured data [15]. However, this approach leads to errors in the imposed spatial gradient, which manifests as errors in the projected field (an example is given in Section III-B).

Here, an alternative method to generate an equivalent source that reproduces time-domain or CW data measured over a plane is demonstrated using gradient-based optimization. The equivalent source can then be used with full-wave models (for example, the open-source k-Wave toolbox [16]) to accurately compute holographic projections through complex media including nonlinearity and heterogeneous material properties.

The problem of calculating an equivalent source has been widely studied in near-field acoustic holography (NAH) [17]. In NAH, an array of microphones is used to measure the

Manuscript received May 15, 2018; accepted July 27, 2018. Date of publication August 1, 2018; date of current version October 3, 2018. This work was supported in part by the Engineering and Physical Sciences Research Council, U.K., under Grant EP/L020262/1, Grant EP/M011119/1, and Grant EP/P008860/1, in part by the European Union's Horizon 2020 Research and Innovation Program H2020 ICT 2016-2017 (as an initiative of the Photonics Public Private Partnership) under Grant 732411, and in part by the Netherlands Organisation for Scientific Research under Grant NWO 613.009.106/2383. *(Corresponding author: Bradley Treeby.)*

B. Treeby, E. Martin, and B. T. Cox are with the Department of Medical Physics and Biomedical Engineering, University College London, London WC1E 6BT, U.K. (e-mail: b.treeby@ucl.ac.uk).

F. Lucka is with the Computational Imaging Group, Centrum Wiskunde & Informatica, 1090 GB Amsterdam, The Netherlands, and also with the Department of Computer Science, University College London, London, U.K.

Digital Object Identifier 10.1109/TUFFC.2018.2861895

output of an acoustic source, typically at audio frequencies. The measurements are made in the near field and consequently capture evanescent waves that decay rapidly with distance from the source. The inversion is formed as a matrix problem, and the operator mapping from the source to the measurement plane is inverted using either singular value decomposition [18], [19] or iterative approaches [20]–[22].

While the framework of NAH is similar to the current problem, an important difference between NAH and acoustic holography in ultrasonics is the ratio of the acoustic wavelength to the separation between the source and the measurement surface. In ultrasonics, the measurement surface will typically be at least 30 mm from the radiating surface, which is 20 wavelengths at 1 MHz in water (and considerably more for higher frequencies and longer measurement distances). This means that the evanescent wave components are not measured. In other words, this paper is concerned with far-field acoustic holography and not with reproducing the evanescent field of a source. Moreover, to capture the width of the ultrasound beam while sampling within the Nyquist limit, the number of measurement points is often on the order of 10 000 or more [5]. The problem sizes thus preclude the use of matrix methods for the calculation of the equivalent source. Here, a similar formulation to that used in NAH is proposed, which is subsequently solved using gradient-based optimization facilitated by numerical forward and adjoint models. Numerical and experimental results using both time-domain and CW sources are then used to demonstrate the approach.

## II. Equivalent Source Calculation Using Gradient-Based Optimization

Consider an acoustic source, such as an ultrasound transducer, which generates a beam of sound in a homogeneous and lossless medium. Suppose that the acoustic pressure is set sufficiently low for nonlinear effects to be negligible, and that acoustic pressure measurements $D$ are made on a plane cutting through a sufficiently narrow part of the beam to allow the whole cross section to be sampled (see [5] for a detailed discussion on measurement conditions for holography).[1]

Now consider a 3-D numerical model of wave propagation in free-space $M$ that takes a source $S$, defined on a plane, and generates the modeled data $M(S)$ on a parallel plane coincident with the measurement positions (see Fig. 1). Note that the position of the source $S$ does not need to match the position of the real source in the experiment—it is merely a device to generate the correct input to the numerical model. The goal is to find the source $\hat{S}$ that generates modeled data $M(\hat{S})$ which matches the measured data $D$ as closely as possible. This can be posed as an optimization problem in which the difference between the modeled data $M(S)$ and the measured data $D$ is minimized, i.e.,

$$\hat{S} = \underset{S}{\operatorname{argmin}}\ \varepsilon(S) \tag{1}$$

[1]This analysis could be generalized to more arbitrary sources, e.g., spherically radiating sources with measurements made on a sphere, but the case described here is the most common in practice.

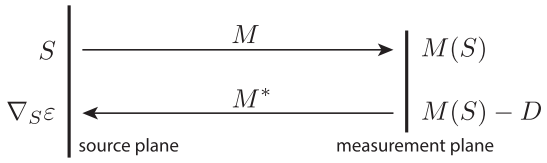


Fig. 1. Mapping between the source plane and the measurement plane using the forward $M$ and adjoint $M^*$ models.

where the error functional $\varepsilon$ is defined here as

$$\varepsilon(S) = \frac{1}{2}\|M(S) - D\|_2^2. \tag{2}$$

This problem is well-posed, given a sufficient-sized measurement plane [5], so a regularization term is not required. This is in contrast to NAH, in which the projection of the evanescent wave components back toward the source is ill-posed.

Here, the minimization problem is solved using gradient descent

$$S^{n+1} = S^n - \eta^n \nabla\varepsilon(S^n) \tag{3}$$

where $n$ is the integer step index, $S^n$ is the source estimate after the $n$th iteration, $\eta^n$ is the step size, and $\nabla\varepsilon(S^n)$ is the gradient of the error functional with respect to each degree of freedom in $S$ [i.e., $S^n$ and $\nabla\varepsilon(S^n)$ have the same dimensions].

In general, the gradient of the error functional is given as

$$\nabla\varepsilon(S) = (M'(S))^*(M(S) - D) \tag{4}$$

where $M'(S)$ is the Fréchet derivative of the wave model $M$ (which is a linearization of $M$ at $S$ that extends the notion of the derivative to functions on Banach spaces [23]) and $A^*$ denotes the adjoint operator of a linear mapping $A$. If the model $M$ is restricted to linear wave propagation, then $M'(S) = M$ and the gradient is given as

$$\nabla\varepsilon(S) = M^*(M(S) - D). \tag{5}$$

For a homogeneous and lossless medium, the adjoint $M^*$ can be calculated using the same numerical wave model $M$ combined with time reversal (or phase conjugation in the CW case) before and after the wave propagation [24]. Thus, each source update is calculated by projecting the current source estimate to the measurement plane, calculating the difference between the modeled and measured data, and then projecting this back to the source plane using time reversal (see Fig. 1). This approach is sometimes called Landweber iteration [23] and can be applied to both time-domain and CW data. Note, while the source optimization is performed assuming a homogeneous and lossless medium, the calculated source plane can subsequently be used to project the field through more complex media, or at higher pressures to simulate nonlinear effects.

To ensure the error $\varepsilon$ is monotonically decreasing while maintaining a reasonable convergence rate, a simple step size adaptation scheme is used to choose $\eta^n$ for each iteration. If the error after the $n$th iteration is increased [i.e., $\varepsilon(S^n) > \varepsilon(S^{n-1})$], the update for $S$ is discarded and $\eta$ is decreased. This is repeated until the error is reduced. For each update step where the error is decreased, the step size for the next iteration

is increased. For the examples presented in Section III, the initial step size was set to 0.5, the step decrement was set to half the current value, and the step increment was set to 1.1 times the current value. While the choice of stopping criterion could be used as a method of regularization for this scheme, such an approach was not necessary and the number of iterations was fixed to between 10 and 30. More sophisticated adaptation schemes could also be used; however, this simple scheme was found to converge sufficiently rapidly for practical purposes.

## III. Validation

### A. Overview

To validate the approach for calculating an equivalent interior source that can recreate data measured on a plane, several simulations were conducted using both CW (single frequency) and time-domain source conditions. The source geometries were based on two Sonic Concepts single-element bowl transducers (Sonic Concepts, Bothell, WA, USA), namely, the H101 and H151. These transducers are widely used in ultrasonics research, particularly for ultrasound therapy. The H101 has a nominal aperture diameter and focal length of 64 mm, while the H151 has a nominal aperture diameter of 64 mm and a focal length of 100 mm. Both transducers can be driven at their fundamental frequency of 1.1 MHz or the third harmonic of 3.3 MHz.

Experimental measurements were conducted using a calibrated 0.2-mm membrane hydrophone in an automated scanning tank (Precision Acoustics, Dorchester, U.K.). The driving signal was generated using a signal generator (33522A, Agilent Technologies, Santa Clara, CA, USA) connected via a 75-W power amplifier (A075, E&I, Rochester, NY, USA) and an impedance matching network. The driving voltage was adjusted to ensure linear propagation, which was verified by examining the spectral content of the focal trace.

To calculate the equivalent source for the CW case, the forward and adjoint models were computed using the acoustic field propagator [25]. This solves the wave equation including a CW mass source in a single step using two fast Fourier transforms (FFTs). For time-domain data, the forward and adjoint models were computed using the 3-D k-space pseudospectral model in the open-source k-Wave toolbox (Version 1.2.1) [11], [12], [16]. The optimization approach described in Section II was coded in MATLAB as a function taking the measured data and returning the equivalent source for a given spatial offset and source plane size. This code will be made freely available as part of a future release of the k-Wave toolbox.

Four examples were considered using both numerical and experimental measured data and both CW and time-domain driving conditions. For comparison, forward projections were also computed using the ASM. The implementation was based on a spectral propagator with angular restriction as described in [26]. For time-domain projections, the input time signal was spectrally decomposed using the FFT and each frequency component was propagated independently. The frequencies were then recombined using an inverse FFT after each spatial step. In each case, the spatial and temporal discretizations used for the ASM matched those used for the k-Wave simulations.

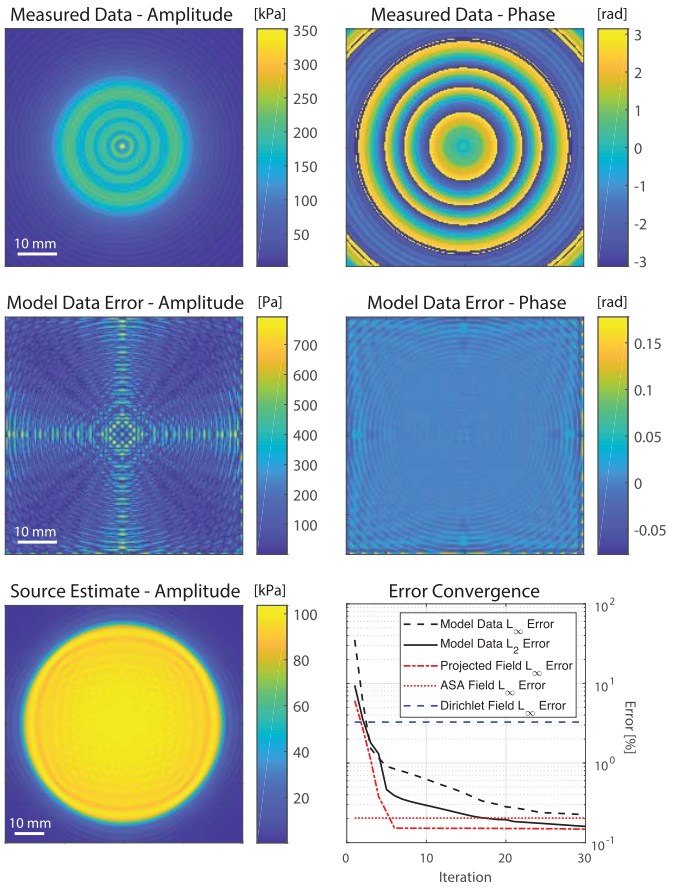


Fig. 2. Top row: amplitude and phase of the numerically measured CW data for the H151 transducer. Middle row: error in the amplitude and phase of the modeled data. Bottom row: calculated source plane and error convergence. The error values after 30 iterations following the entries in the plot legend are 0.255%, 0.160%, 0.148%, 0.204%, and 3.27%, respectively.

### B. Continuous-Wave Sources

In the first example, the measured data were generated numerically (to provide a ground truth) using the fast near-field method in the FOCUS toolbox [27], [28]. The source geometry was based on the H151 transducer, with a frequency of 1.1 MHz, CW driving conditions, and a surface pressure of 100 kPa. A measurement plane with dimensions 60 × 60 mm with a point spacing of 0.3 mm was acquired 45 mm from the rear surface of the bowl. The optimization approach described in Section II was then used to calculate an equivalent interior source distributed over an $80 \times 80$ mm plane positioned at the back of the bowl (i.e., 45 mm from the measured plane).

Fig. 2 shows the amplitude and phase of the measured CW data from FOCUS, the error in the amplitude and phase of the modeled data after the 30th iteration of the optimization, and the calculated source plane. In the plane of the measured data, the amplitude and phase differences between the measured and modeled data are small, with the largest errors evident at the edge of the field. Fig. 2 also shows the relative $L_2$ and $L_\infty$ error norms between the measured and modeled data after each

iteration of the optimization, as well as the corresponding error in the projected field calculated using the source estimate after each iteration. The error initially reduces very rapidly with all error norms less than 1% after five iterations. With further iterations, the model error continues to decrease, but at a much slower rate, while the error in the projected field remains constant. The error floor in the projected field is marginally smaller than the error obtained using the ASM (dotted line in Fig. 2). For these source conditions, the ASM can be considered the gold standard for holographic projections.

For comparison, the measured CW data were also projected using the 3-D k-space pseudospectral model in the open-source k-Wave toolbox using the `source.p_mode = 'dirichlet'` option. At each time step, this replaces the pressure values over the measurement plane with the measured data. However, this data replacement at discrete time steps does not preserve the spatial gradients that existed in the original field and thus introduces numerical errors. (Note, this is not unique to k-Wave and also applies to other collocation methods including those based on finite differences.) For a Courant–Friedrichs–Lewy (CFL) number of 0.1, the relative $L_\infty$ error is 3.27%, which is more than 20 times larger than the equivalent source approach. When the CFL is reduced to 0.025, the error is reduced only slightly to 3.02%. Thus, this error does not converge away with practical numbers of time steps. This motivates the use of the equivalent source approach proposed in this paper.

Fig. 3 shows the amplitude of the wave field in a 2-D slice through the focal point calculated using FOCUS. The corresponding error in the projected field calculated using k-Wave with the optimized equivalent-source plane after the 30th iteration and the Dirichlet source option with the measured data and two different CFLs is also shown. For the projection using the equivalent source, the absolute errors are very small, particularly on the beam axis, with the largest errors at the edge of the field, where the acoustic pressure is low. In comparison, the errors using the Dirichlet source option are much larger, particularly in the focal region.

In the second example, the measured data were experimentally acquired using the H101 transducer. This was driven at 3.3 MHz using a 40 cycle burst, with a CW signal acquired in a time window after the field had reached a steady state. A measurement plane with dimensions 45 × 45 mm with a point spacing of 0.2 mm was measured 40 mm from the rear surface of the bowl. The corresponding source plane was 80 × 80 mm. Figs. 4 and 5 show the analogous information to Figs. 2 and 3. In this case, the ASM was used as the ground truth for the projected field. Again, the error converges very rapidly. After six iterations, the difference in the projected field compared to the ASM was less than 0.2%. Thus, the approach also works robustly for experimental data, which contains noise.

### C. Broadband Sources

In the third example, time-domain measured data were generated numerically using k-Wave. The source geometry was based on the H101 transducer and was modeled using a grid-based discrete bowl [29]. The transducer was driven by a four-cycle tone-burst with a center frequency of 1.1 MHz and a surface pressure of 100 kPa. A measurement plane with dimensions 45 × 45 mm with a point spacing of 0.3 mm was numerically acquired 40 mm from the rear surface of the bowl. The optimization approach described in Section II was then used to calculate a time-varying interior source distributed over a 90 × 90 mm plane positioned at the back of the bowl.

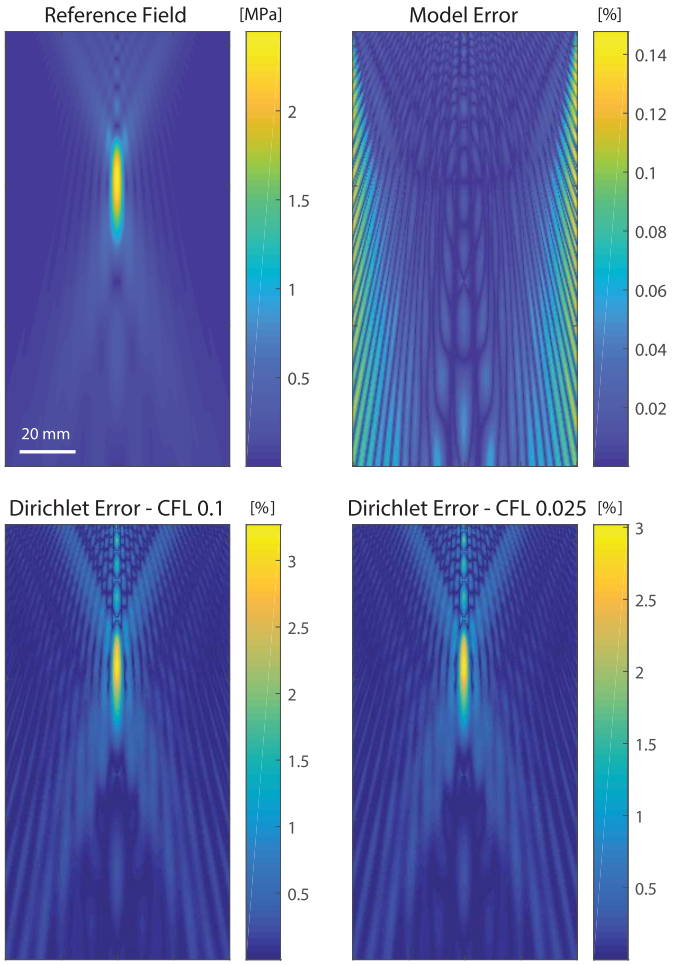


Fig. 3. Top row: beam pattern calculated using the fast-near-field method (left) and error in the projected field calculated using the optimized source plane (right) for the H151 transducer. The transducer is positioned at the top of the image. Bottom row: error in the projected field when using k-Wave with the Dirichlet source option for two different CFL numbers.

Fig. 6 shows a maximum intensity projection (MIP) through the time-domain measured data from k-Wave, an MIP through the error in the modeled data after the 20th iteration of the optimization, and an MIP through the calculated time-domain source plane. In the plane of the measured data, the absolute errors are small, although slightly larger than in the CW case. The increased error at the central point is due to a slight phase error in the edge waves arriving from the outer edge of the transducer, which coherently sum at the central point. This is shown in Fig. 7, which shows time traces from the central point (largest error approximately 8%), and a point offset by 3 mm or 10 samples (largest error approximately 1%). Although the traces for the central point are qualitatively

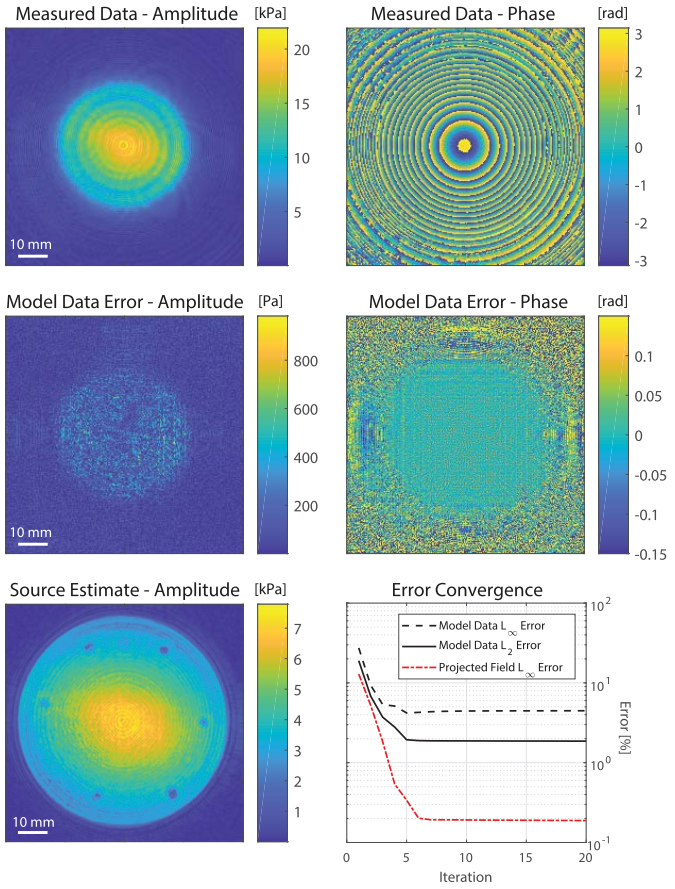


Fig. 4. Top row: amplitude and phase of the experimentally measured CW data for the H101 transducer. Middle row: error in the amplitude and phase of the modeled data. Bottom row: calculated source plane and error convergence with iteration number. The error values after 20 iterations following the entries in the plot legend are 4.47%, 1.87%, and 0.190%, respectively.

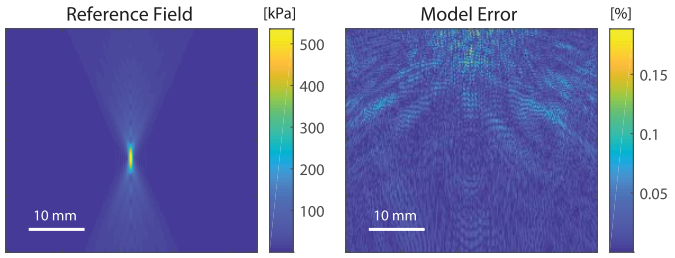


Fig. 5. Beam pattern calculated using the ASM (left) and error in the projected field calculated using the optimized source plane (right) for the H101 transducer. The transducer is positioned at the top of the image.

similar, the small phase offset results in an increase in the error metric. Fig. 6 also shows the relative $L_2$ and $L_\infty$ error norms between the measured and modeled data after each iteration of the optimization. Again, the error reduces very rapidly, with little improvement after five iterations.

Fig. 8 shows an MIP through the time-domain data in the central 2-D slice calculated using k-Wave with the true source conditions, and the corresponding error in the projected field calculated using k-Wave with the optimized equivalent-source plane after the 20th iteration. The corresponding time traces from the focal point (position of the highest pressure) are

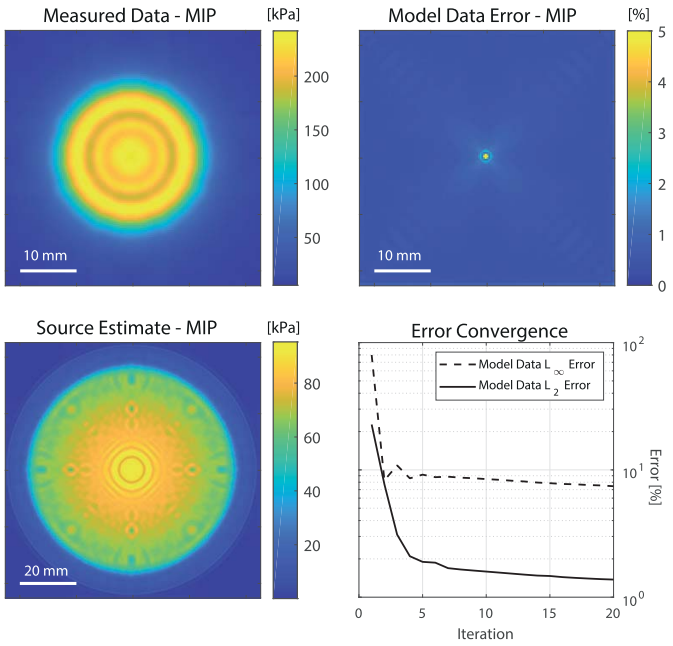


Fig. 6. Top row: MIPs through the numerically measured time-domain data for the H151 transducer and the error in the modeled data. Bottom row: MIP through the source estimate and error convergence with iteration number. The $L_\infty$ and $L_2$ error values after 20 iterations are 7.44% and 1.37%, respectively.

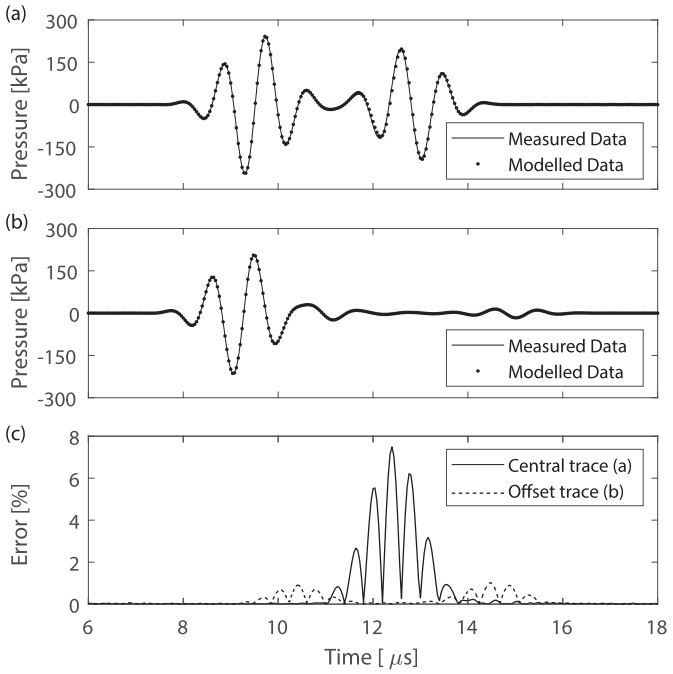


Fig. 7. Time-domain traces from the measured and modeled data shown in Fig. 6. (a) Central trace. (b) Trace offset from the center by 3 mm or 10 samples. (c) Relative error.

shown in Fig. 9. Again, the absolute errors are very small. For comparison, the error in the focal trace calculated using the ASM is also shown and is of a similar order of magnitude.

In the fourth example, the measured data were experimentally acquired using the H151 transducer driven at 1.1 MHz by a four-cycle burst. A measurement plane with dimensions

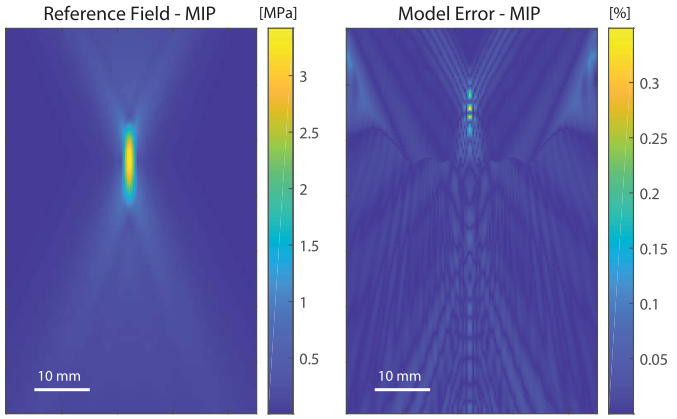


Fig. 8. Time-domain MIP through the beam pattern calculated using k-Wave (left) and error in the projected field calculated using the optimized source plane (right) for the H101 transducer. The transducer is positioned at the top of the image.

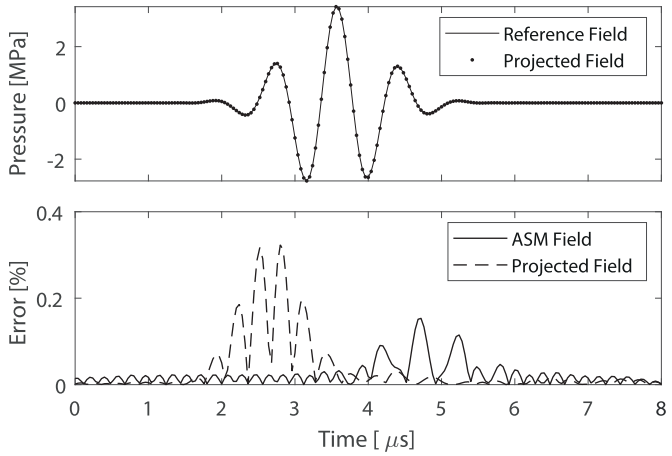


Fig. 9. Time-domain traces at the focal position calculated from the reference field and the projected field using the optimized equivalent source for the source shown in Fig. 6. The relative error between the two profiles and the relative error in the focal trace calculated using the ASM are also shown.

60 × 60 mm with a point spacing of 0.3 mm was measured 45 mm from the rear surface of the bowl. The corresponding source plane was 80 × 80 mm. Figs. 10 and 11 show the analogous information to Figs. 6 and 7. In this case, the ASM was used as the ground truth for the projected field. Again, the error converges very rapidly, with little improvement after four iterations. Although the absolute errors are larger (see Fig. 11), the optimized equivalent source successfully reproduces most of the features in the measured data. A plot of the axial peak pressure through the projected field using the optimized equivalent source and ASM is shown in Fig. 12, with the differences less than 1%. Note, the six small circles visible on the source estimate in Figs. 4 and 10 are part of the bonding from the piezoelectric element [29].

### *D. Projection Through Complex Media*

To demonstrate the utility of calculating an equivalent source more generally, i.e., mapping from a Dirichlet boundary condition to an interior source, the calculated

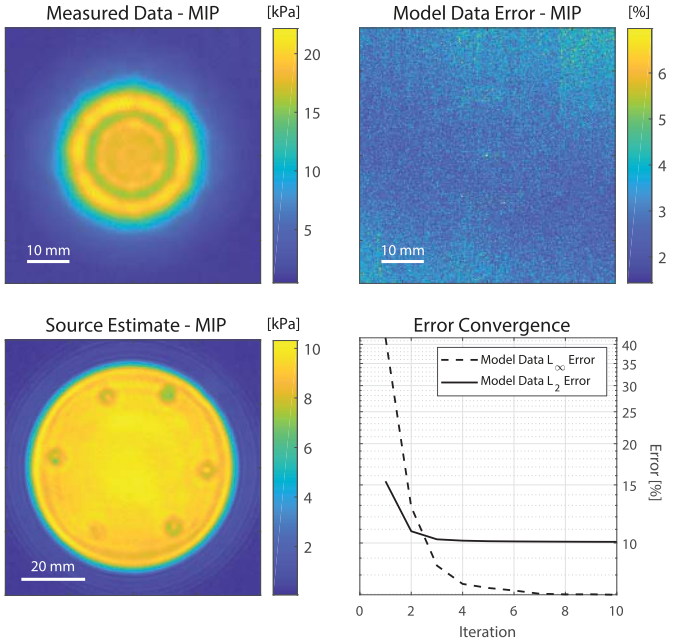


Fig. 10. Top row: MIPs through the experimentally measured time-domain data for the H101 transducer and the error in the modeled data. Bottom row: MIP through the source estimate and error convergence with iteration number. The $L_\infty$ and $L_2$ error values after 10 iterations are 6.97% and 10.1%, respectively.

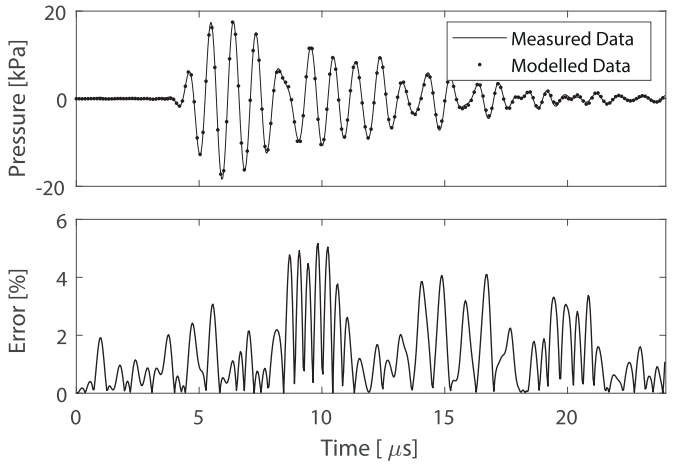


Fig. 11. Time-domain trace at the center of the measured plane from the measured and modeled data shown in Fig. 10. The relative error between the two profiles is also shown.

equivalent-source plane for the experimental measurement of the H101 transducer shown in the bottom panel of Fig. 4 was used to project the ultrasound field through a heterogeneous nonlinear medium. The simulation was conducted using the k-space pseudospectral method in the k-Wave toolbox [11], [12]. The spatially varying maps of sound speed, density, nonlinearity, and absorption coefficient were derived from the AustinWoman voxel model [30] using book values for the segmented regions. The focal position of the transducer was placed in the liver using a window between the ribs. A map of the peak positive pressure in the central plane overlaid on the sound speed map is shown in Fig. 13. In this

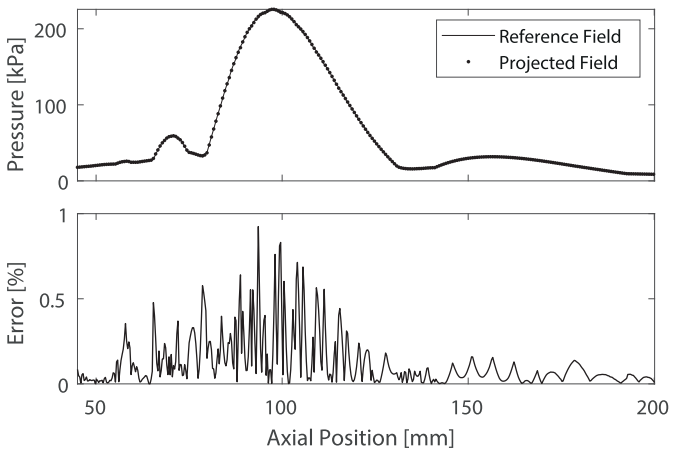


Fig. 12. Temporal peak positive pressure along the beam axis of the transducer calculated using the ASM (reference field) and k-Wave along with the optimized equivalent source (projected field). The relative error between the two profiles is also shown.

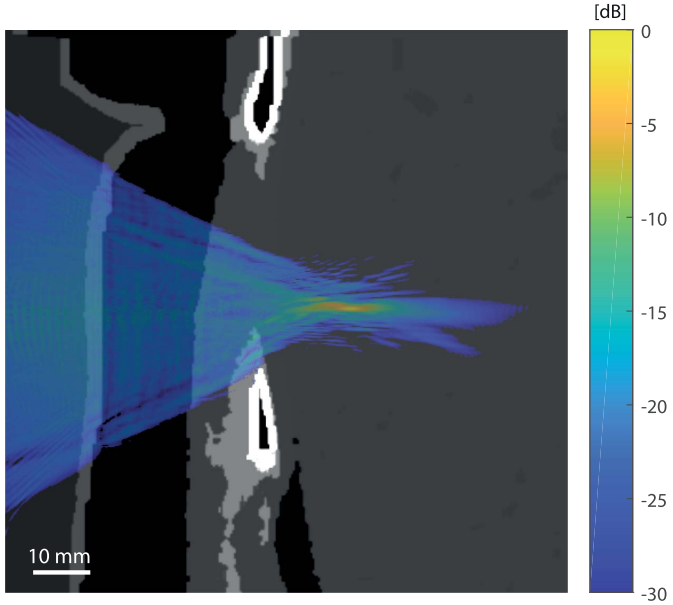


Fig. 13. Central plane through the ultrasound field calculated using the optimized source plane shown in Fig. 4 in a heterogeneous medium. The peak positive pressure is shown overlaid on the sound speed map.

case, the beam pattern has undergone significant aberration due to the overlying tissue and the muscle layers surrounding the rib cage.

## IV. Conclusion

A general method for calculating an interior source that accurately reproduces a measured plane is proposed based on numerical optimization. This is particularly useful for computing holographic projections using full-wave models that include the effects of nonlinearity and heterogeneous media. The formulation is similar to that used for NAH, but is solved using alternate numerical approaches due to the large-scale nature of the inverse problem. The update steps are calculated using gradient descent, where the gradients of the error functional are calculated using a numerical forward model and its adjoint. The approach is demonstrated to work robustly for both time-domain and CW data using both numerical and experimental measurements. For the examples shown here, the optimization converges within six update steps (i.e., 12 runs of the forward model). In the future, the approach could be generalized to nonplanar or sparse measurement data, or a forward model that includes the effects of nonlinearity and absorption in the calculation of the equivalent source.

## References

[1] P. R. Stepanishen and K. C. Benjamin, "Forward and backward projection of acoustic fields using FFT methods," *J. Acoust. Soc. Amer.*, vol. 71, no. 4, pp. 803–812, 1982.

[2] J. D. Maynard, E. G. Williams, and Y. Lee, "Nearfield acoustic holography: I. Theory of generalized holography and the development of NAH," *J. Acoust. Soc. Amer.*, vol. 78, no. 4, pp. 1395–1413, 1985.

[3] G. T. Clement and K. Hynynen, "Field characterization of therapeutic ultrasound phased arrays through forward and backward planar projection," *J. Acoust. Soc. Amer.*, vol. 108, no. 1, pp. 441–446, 2000.

[4] Y. Jing *et al.*, "Experimental verification of transient nonlinear acoustical holography," *J. Acoust. Soc. Amer.*, vol. 133, no. 5, pp. 2533–2540, 2013.

[5] O. A. Sapozhnikov, S. A. Tsysar, V. A. Khokhlova, and W. Kreider, "Acoustic holography as a metrological tool for characterizing medical ultrasound sources and fields," *J. Acoust. Soc. Amer.*, vol. 138, no. 3, pp. 1515–1532, 2015.

[6] T. D. Mast, L. M. Hinkelman, M. J. Orr, V. W. Sparrow, and R. C. Waag, "Simulation of ultrasonic pulse propagation through the abdominal wall," *J. Acoust. Soc. Amer.*, vol. 102, no. 2, pp. 1177–1190, 1997.

[7] H.-L. Liu, N. McDannold, and K. Hynynen, "Focal beam distortion and treatment planning in abdominal focused ultrasound surgery," *Med. Phys.*, vol. 32, no. 5, pp. 1270–1280, 2005.

[8] V. Suomi, J. Jaros, B. Treeby, and R. O. Cleveland, "Full modeling of high-intensity focused ultrasound and thermal heating in the kidney using realistic patient models," *IEEE Trans. Biomed. Eng.*, vol. 65, no. 5, pp. 969–979, May 2018.

[9] G. F. Pinton, J. Dahl, S. Rosenzweig, and G. E. Trahey, "A heterogeneous nonlinear attenuating full-wave model of ultrasound," *IEEE Trans. Ultrason., Ferroelectr., Freq. Control*, vol. 56, no. 3, pp. 474–488, Mar. 2009.

[10] E. Bossy and Q. Grimal, "Numerical methods for ultrasonic bone characterization," in *Bone Quantitative Ultrasound*, P. Laugier and G. Haiat, Eds. Dordrecht, The Netherlands: Springer, 2011, pp. 181–228.

[11] B. E. Treeby, J. Jaros, A. P. Rendell, and B. T. Cox, "Modeling nonlinear ultrasound propagation in heterogeneous media with power law absorption using a *k*-space pseudospectral method," *J. Acoust. Soc. Amer.*, vol. 131, no. 6, pp. 4324–4336, 2012.

[12] J. Jaros, A. P. Rendell, and B. E. Treeby, "Full-wave nonlinear ultrasound simulation on distributed clusters with applications in high-intensity focused ultrasound," *Int. J. High Perform. Comput. Appl.*, vol. 30, no. 2, pp. 137–155, 2016.

[13] M. H. Carpenter, D. Gottlieb, and S. Abarbanel, "Time-stable boundary conditions for finite-difference schemes solving hyperbolic systems: Methodology and application to high-order compact schemes," *J. Comput. Phys.*, vol. 111, no. 2, pp. 220–236, 1994.

[14] B. E. Treeby, E. Z. Zhang, and B. T. Cox, "Photoacoustic tomography in absorbing acoustic media using time reversal," *Inverse Problems*, vol. 26, no. 11, p. 115003, 2010.

[15] M. Tanter, J.-L. Thomas, F. Coulouvrat, and M. Fink, "Breaking of time reversal invariance in nonlinear acoustics," *Phys. Rev. E, Stat. Phys. Plasmas Fluids Relat. Interdiscip. Top.*, vol. 64, no. 1, p. 016602, 2001.

[16] B. E. Treeby and B. T. Cox, "k-Wave: MATLAB toolbox for the simulation and reconstruction of photoacoustic wave fields," *J. Biomed. Opt.*, vol. 15, no. 2, p. 021314, 2010.

[17] E. G. Williams and J. D. Maynard, "Holographic imaging without the wavelength resolution limit," *Phys. Rev. Lett.*, vol. 45, no. 7, pp. 554–557, 1980.

[18] W. A. Veronesi and J. D. Maynard, "Digital holographic reconstruction of sources with arbitrarily shaped surfaces," *J. Acoust. Soc. Amer.*, vol. 85, no. 2, pp. 588–598, 1989.

[19] A. Sarkissian, "Method of superposition applied to patch near-field acoustic holography," *J. Acoust. Soc. Amer.*, vol. 118, no. 2, pp. 671–678, 2005.

[20] N. Valdivia and E. G. Williams, "Krylov subspace iterative methods for boundary element method based near-field acoustic holography," *J. Acoust. Soc. Amer.*, vol. 117, no. 2, pp. 711–724, 2005.

[21] J. Hald, "Fast wideband acoustical holography," *J. Acoust. Soc. Amer.*, vol. 139, no. 4, pp. 1508–1517, 2016.
[22] E. Fernandez-Grande, A. Xenaki, and P. Gerstoft, "A sparse equivalent source method for near-field acoustic holography," *J. Acoust. Soc. Amer.*, vol. 141, no. 1, pp. 532–542, 2017.
[23] C. R. Vogel, *Computational Methods for Inverse Problems*. Philadelphia, PA, USA: SIAM, 2002.
[24] S. R. Arridge, M. M. Betcke, B. T. Cox, F. Lucka, and B. E. Treeby, "On the adjoint operator in photoacoustic tomography," *Inverse Problems*, vol. 32, no. 11, p. 115012, 2016.
[25] B. E. Treeby, J. Budisky, E. S. Wise, J. Jaros, and B. T. Cox, "Rapid calculation of acoustic fields from arbitrary continuous-wave sources," *J. Acoust. Soc. Amer.*, vol. 143, no. 1, pp. 529–537, 2018.
[26] X. Zeng and R. McGough, "Evaluation of the angular spectrum approach for simulations of near-field pressures," *J. Acoust. Soc. Amer.*, vol. 123, no. 1, pp. 68–76, Jan. 2008.
[27] J. F. Kelly and R. J. McGough, "Transient fields generated by spherical shells in viscous media," in *Proc. 8th Int. Symp. Therapeutic Ultrasound*, vol. 1113, 2009, pp. 210–214. [Online]. Available: https://aip.scitation.org/doi/abs/10.1063/1.3131415
[28] D. Chen and R. J. McGough, "A 2D fast near-field method for calculating near-field pressures generated by apodized rectangular pistons," *J. Acoust. Soc. Amer.*, vol. 124, no. 3, pp. 1526–1537, 2008.
[29] E. Martin, Y. T. Ling, and B. E. Treeby, "Simulating focused ultrasound transducers using discrete sources on regular Cartesian grids," *IEEE Trans. Ultrason., Ferroelectr., Freq. Control*, vol. 63, no. 10, pp. 1535–1542, Oct. 2016.
[30] J. W. Massey and A. E. Yilmaz, "AustinMan and AustinWoman: High-fidelity, anatomical voxel models developed from the VHP color images," in *Proc. 38th Annu. Int. Conf. IEEE Eng. Med. Biol. Soc. (EMBC)*, 2016, pp. 3346–3349, doi: 10.1109/EMBC.2016.7591444.

**Bradley Treeby** (M'13), photograph and biography not available at the time of publication.

**Felix Lucka**, photograph and biography not available at the time of publication.

**Eleanor Martin**, photograph and biography not available at the time of publication.

**B. T. Cox**, photograph and biography not available at the time of publication.